catalysts

MDPI

Article

Synthesis, Characterization and Dye Removal Capability of Conducting Polypyrrole/$Mn_{0.8}Zn_{0.2}Fe_2O_4$/Graphite Oxide Ternary Composites

Mohamed A. Gabal [1,2,*], Enam A. Al-Harthy [1,3], Yasser M. Al Angari [1], Mohamed Abdel Salam [1], Ayman Awad [2], Amany A. Al-Juaid [3] and Abdu Saeed [4]

[1] Chemistry Department, Faculty of Science, King Abdulaziz University, Jeddah 21589, Saudi Arabia
[2] Chemistry Department, Faculty of Science, Benha University, Benha 30311, Egypt
[3] Chemistry Department, Faculty of Science, University of Jeddah, Jeddah 21959, Saudi Arabia
[4] Physics Department, Faculty of Science, King Abdulaziz University, Jeddah 21959, Saudi Arabia
* Correspondence: mgabalabdonada@yahoo.com; Tel.: +966-557-071-572

Abstract: Herein, ternary composites from polypyrrole (PPy), $Mn_{0.8}Zn_{0.2}Fe_2O_4$ (MZF), and graphite oxide (GO) were prepared to remove acid red dye (AR1) from wastewater. MZF was synthesized using spent Zn–C batteries, acid leaching, and sucrose auto-combustion processes; GO was prepared via oxidation and exfoliation of graphite. The composites were prepared by adding MZF and GO during the in-situ polymerization of pyrrole. Different PPy/MZF/GO (PMG) composites were prepared by changing the weight ratios of the PPy, MZF, and GO. We investigated the prepared composites' structural, magnetic, and electrical/dielectric properties. We evaluated different experimental conditions' influences on dye removal performance, such as pH, dosage, dye concentration, temperature, and contact time. XRD, FT-IR, and magnetic properties indicated that PPy completely coated the other contents. The electrical/dielectric properties improved while increasing the GO ratio. The PMG at GO content 50 wt.% (PMG50) showed the most efficient ratio for better removing AR1 from wastewater.

Keywords: PPy/$Mn_{0.8}Zn_{0.2}Fe_2O_4$/GO; ternary composites; conductivity; dye removal; coating

Citation: Gabal, M.A.; Al-Harthy, E.A.; Al Angari, Y.M.; Abdel Salam, M.; Awad, A.; Al-Juaid, A.A.; Saeed, A. Synthesis, Characterization and Dye Removal Capability of Conducting Polypyrrole/$Mn_{0.8}Zn_{0.2}Fe_2O_4$/Graphite Oxide Ternary Composites. *Catalysts* **2022**, *12*, 1624. https://doi.org/10.3390/catal12121624

Academic Editor: Shuhui Sun

Received: 13 November 2022
Accepted: 8 December 2022
Published: 10 December 2022

1. Introduction

Using organic dyes and pigments in many industries, such as textiles, leather, dyestuff, paper, and food, generates a massive amount of colored wastewater [1]. Discharging of such waters, even with small amounts of these highly toxic and carcinogenic contaminants, in aquatic environments, results in their accumulation in living organisms since they are difficult to decompose under natural conditions. Many methods have been developed to exclude these wastes, including ion exchange, membrane separation, photo-catalysis, filtration, biodegradation, adsorption, etc. [2–7]. Among these techniques, adsorption, mainly depending on magnetic separation, was proven to be the most reliable and promising due to its simplicity, cheapness, high efficiency, easy separability, and environment [8–10].

Ferrites nanoparticles have been successfully applied to remove different dyes from wastewater depending on their high removal capacity, large surface area, and surface electrostatic charge interactions with dyes [11–14]. For further adsorption enhancement, surface-functionalized organic and inorganic ferrite magnetic adsorbents have caught the interest of many investigators.

Wu et al. [15] synthesized poly acrylic acid/$MnFe_2O_4$ nanocomposites for methylene blue (MB) dye adsorption. Meng et al. [16] prepared chitosan-modified $MnFe_2O_4$ nanoparticles to remove Cu^{2+} ions. Oyetade et al. [17] developed carbon nanotube/$CoFe_2O_4$ to investigate their adsorption capability for rhodamine B. Gabal et al. studied the adsorption capability of malachite green and acid red dye (AR1) using $CoFe_2O_4$ nanocomposites with

graphene [18], multi-walled carbon nanotubes [19], and polyaniline [20]. Additionally, they investigated the adsorption removal of crystal violet dye using $Mn_{0.8}Zn_{0.2}Fe_2O_4$ nanoparticles [21].

Graphite oxide (GO), with two-dimensional carbon sheet sp2 networks, having enormous applications in many fields, could be produced on a large scale via chemical oxidation and exfoliation of graphite [2]. The existence of delocalized p-electrons, despite a sufficient percentage of oxygen-containing functional groups on its surfaces, could facilitate the adsorption removal of many environmental contaminants [22]. Additionally, the polypyrrole (PPy) conducting polymer has attracted much interest due to its high conductivity, as well as its excellent adsorption property for dyes via their chelation to the amine groups of the polymer chains [23,24].

Such ternary hybrid composites, PPy/ferrites/GO, were thoroughly investigated in the literature for their different properties to highlight possible promising applications in various fields. Ding et al. [25] synthesized $CoFe_2O_4$/PPy/graphene oxide composites for potential applications in broadband microwave absorption. Mariappan et al. [26] studied the electrochemical properties of reduced graphene oxide/PPy/$CoFe_2O_4$ nanocomposites for hybrid aqueous supercapacitors applications. Hussain et al. [27] prepared different concentrations of GO/$NiFe_2O_4$/PPy dielectric nanocomposites for energy storage applications. Riaz et al. [28] prepared GO/$MnFe_2O_4$/PPy nanocomposites and checked them for energy storage, and capacitive applications. Thu et al. [29] developed graphene-$MnFe_2O_4$-PPy ternary hybrids for high-performance supercapacitor electrodes.

Considering the unique advantages of ferrites, GO, and PPy materials in dyes' adsorption removal processes, combining these materials in one composite could suggest unusual properties compared to what each has alone. However, to the best of our knowledge, the use of PPy/ferrite/GO ternary hybrid composites in dyes' adsorption removal processes was seldom studied. Therefore, in this work, we synthesized ternary composites from PPy, $Mn_{0.8}Zn_{0.2}Fe_2O_4$ (MZF), and GO at different weight ratios for the AR1's removal from aqueous solutions. In addition, the structural, morphological, and electromagnetic properties of the PPy/MZF/GO (PMG) ternary composites were investigated. MZF was processed using materials from spent Zn–C batteries (SZCBs) via acid leaching and sucrose auto-combustion routes [30]. The GO was synthesized via graphite oxidation, and exfoliation of graphite using Hummer's method [31]. The ternary composites were then prepared by adding MZF and GO contents during the in situ polymerization of pyrrole [32].

2. Results and Discussion

2.1. XRD

Figure 1 displays the XRD characterization of prepared GO, PPy, and PMG composites with different ratios. The graphite oxidation product indicated a strong peak at 10.4°, which could be assigned to the (001) reflection plane of GO [33], along with a very small intensity broad one at 26.6°. This small peak could correspond to the (002) reflection plane of graphite restored as an impurity [34]. On the other hand, the XRD pattern of prepared PPy showed a very broad peak centered at 25°, ascribed to the amorphous oriented polymer chain having perpendicular periodicity [29,35–37].

The XRD of PMG composites exhibited only the very broad peak characteristic of PPy, without any indication of the presence of MZF or GO. The disappearance of the ferrite's diffraction peaks [30] could be attributed, as discussed in our previous publication on MZF/PPy composites [38], to the core-shell's formation in which the amorphous PPy shell completely coated the MZF (acted as core). In addition, the obvious disappearance of the (001) characteristic peak of GO indicated the complete exfoliation, accompanied by the coating of the GO stacked layers during the in situ polymerization process of the PPy matrix [28,39]. As a result, the obtained XRD, could thus provide quite convincing evidence for both MZF and GO to be coated by PPy.

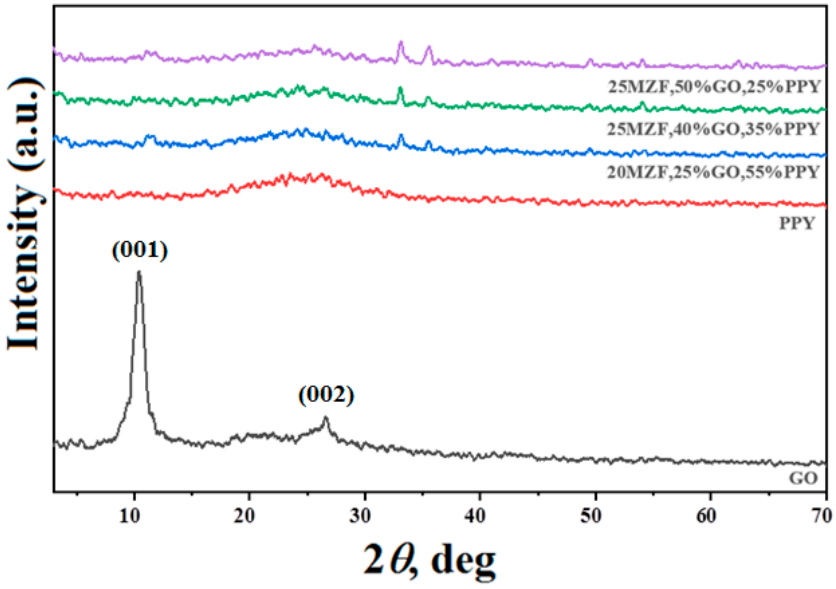

Figure 1. XRD patterns of graphite oxidation product, pure PPy, and PMG composites with different ratios.

The most crucial and obvious point here is that the diffraction pattern is not affected by the compositional ratio even with the smallest percentage of PPy, where its amorphous characteristics become predominant. The two tiny peaks that appeared at 33 and 35.6° could be assigned, as in our previous publication [38], to the most intense peak (311) of the ferrite spinel, and some interactions between PPy and MZF.

2.2. FT-IR

Figure 2 shows the FT-IR spectra of pure PPy, GO, and PMG composites with different compositional ratios. The PPy peaks could be assigned as in the published work [16]. In PPy, the bands that appeared at 3450 and 1637 cm^{-1} could be attributed to N-H and C=N stretching vibrations, respectively. The small bands observed at 1545 and 1455 cm^{-1} were assigned to the pyrrole ring's asymmetric and symmetric C=C stretching vibration. The bands that appeared at 1290, 1170, and 1040 cm^{-1} were assigned to in-plane deformation C-H, while others at 899 and 782 cm^{-1} were assigned to the out-of-plane deformation [38]. The strong band at 1637 cm^{-1} for GO could be assigned as the C-O stretching vibration attributed to the graphite oxidation [26].

FT-IR of all PMG composites indicated similar bands to that attributed to the pure PPy. Interestingly, the two characteristic bands attributed to the stretching vibration in both octahedral and tetrahedral lattice sites of cubic ferrite spinels, which generally appear in the range of 400–600 cm^{-1}, completely disappeared at all ratios. This behavior confirms the core-shell formation, and the complete inclusion of GO and MZF materials inside the PPy matrix in accordance with the obtained XRD results. The compositional ratios also do not affect the type of the obtained bands, indicating the predomination of the PPy structure on the other enclosed components.

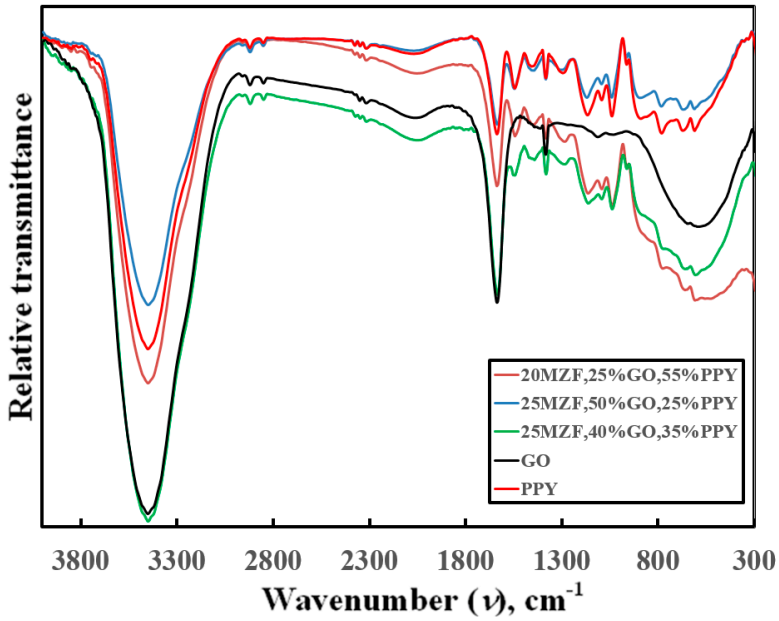

Figure 2. FT-IR spectra of graphite oxidation product, pure PPy, and PMG composites with different ratios.

2.3. TEM

The TEM study further confirmed the complete inclusion of the GO and MZF in the PPy matrix. Figure 3 exhibits TEM images of PPy, GO, and PMG25 composite as a typical image. The PPy (Figure 3a) showed spherically shaped macromolecules that are loosely compacted [40]. The GO image (Figure 3b) indicated ultrathin exfoliated transparent layers having strong surface wrinkles. Figure 3c presents the TEM image of the PMG25 composite, which shows the complete coating and embedding of MZF particles and GO layers inside the PPy matrix.

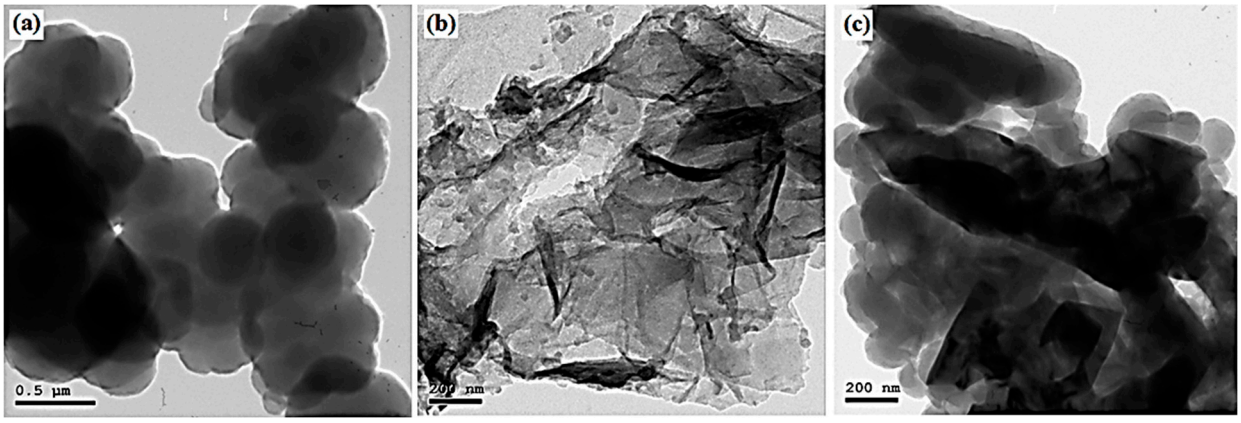

Figure 3. TEM images of (**a**) graphite oxidation product, (**b**) pure PPy, and (**c**) PMG25 composite.

The presence of MZF particles during the sonication process of GO hinders their layer stacking and facilitates the GO layers' separation [18], resulting in the disappearance of the GO characteristic XRD peaks, as discussed through XRD measurements. The in situ polymerization process of PPy on GO surfaces enlarges this separation. The absence of any MZF particles in the image assures the core-shell formation. Additionally, the surface darkness obtained suggested anchoring the MZF particles on the GO layers prior to the in situ polymerization and core-shell formation. In general, TEM images show accumulated

particles that connect with each other, and this accumulation could be due to magnetic interactions [41].

2.4. Magnetic Properties

Figure 4 shows the magnetic hysteresis loops of the prepared PMG ternary composites. The obtained saturation magnetization (M_s) results (Table 1) indicated very weak magnetic characters of all the samples; these results agreed well with the expected non-magnetic characteristics of PPy and GO. This almost disappearance of the magnetic properties of the MZF component confirms the core-shell behavior discussed before in XRD and FT-IR results. It was reported that the concentration of the non-magnetic cations at the B-site could lead to a low magnetic moment, and subsequently low magnetization [42]. However, here, the complete coating of MZF by the non-magnetic PPy matrix causes the magnetic characteristics of MZF to vanish. It can be seen (Figure 4 and Table 1) that there are apparent differences in the obtained saturation magnetization with different compositional ratios (PMG50 > PMG40 > PMG25); this result could be discussed in view of the compositional percentages of MZF and PPy components. The larger magnetizations were obtained with the composites with higher MZF and lower PPy contents (PMG50, PMG40). Increasing the PPy range (PMG25) is expected to increase the non-magnetic PPy shell coated in the MZF core, and consequently reduce the magnetization.

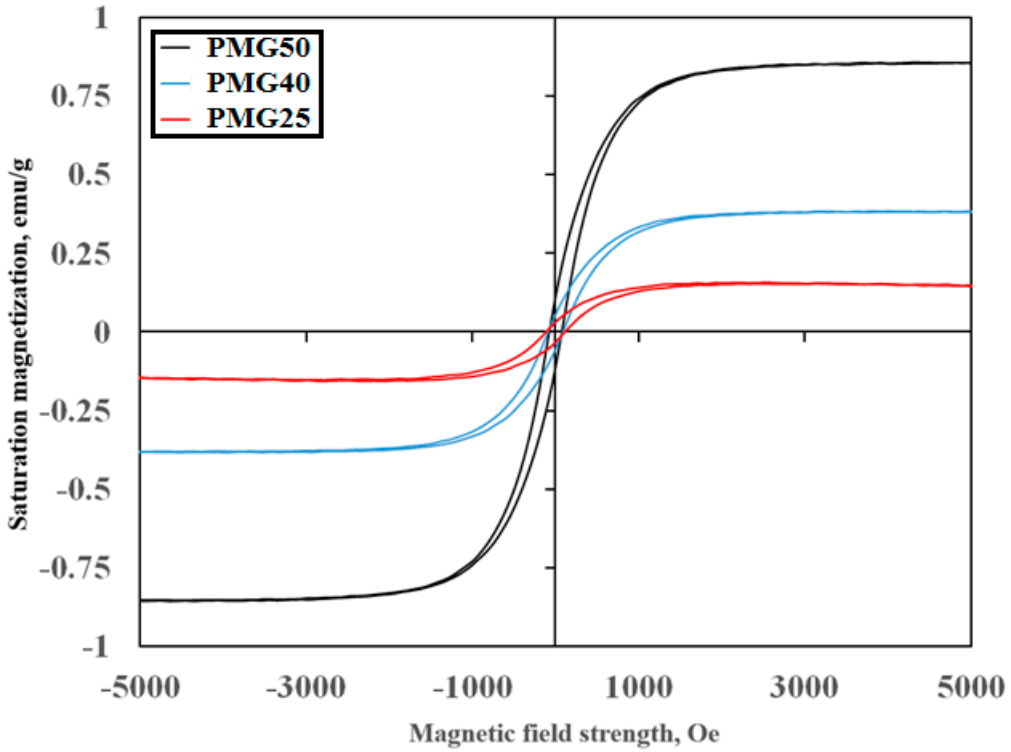

Figure 4. Hysteresis loops of the studied PMG composites at different ratios.

Table 1. Magnetic and electrical properties of PPy and PMG composites.

Material	M_S (emu/g)	σ, (ohm^{-1} cm^{-1})
Pure PPy	-	8.8×10^{-3}
PMG25	0.157	1.8×10^{-2}
PMG40	0.383	1.9×10^{-2}
PMG50	0.857	2.7×10^{-2}

2.5. Electrical Properties

Figure 5 represents the change in ac-conductivity with temperature at different applied frequencies for prepared pure PPy, alongside the prepared PMG50, PMG40 > PMG25 composites. The figure shows that all the samples exhibited metallic conductivity and showed constant conductivity with increasing temperature. The obvious decrease in the conductivity, with increasing frequency, could be discussed in view of the inability of charge carriers to rotate themselves with increasing frequencies [38]. The observed decrease in conductivity, over 420 K in PMG composites, indicated the initiation of the chain decomposition of GO as well as PPy [29]. The presence of GO and MZF thus appeared to catalyze the PPy decomposition. The coating of the PPy, for both MZF and GO, increases the exposed surface area of PPy, and thus facilitates its decomposition at lower temperatures [38].

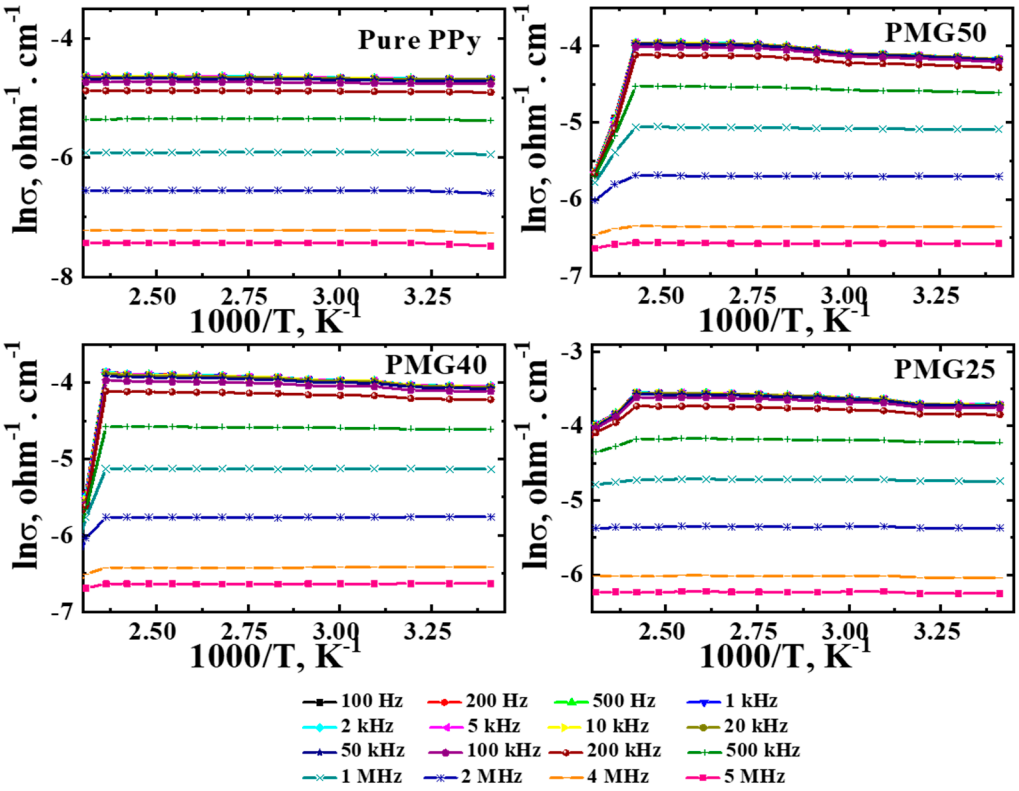

Figure 5. Ac-conductivity versus 1000/*T* for pure PPy and PMG composites with different ratios.

Comparing the conductivity values measured at 400 K and 100 kHz (Table 1) for pure PPy and PMG composites indicated higher conductivity values for PMG composites than for pure PPy. In addition, the conductivity value was observed to increase with increasing PPy ratio in the composites. The possible persuading reason for this behavior is that including the conducting GO in the PPy matrix would increase the conductivity. Additionally, the increase in the conductor PPy ratio in the PMG composites is accompanied by the decrease in the ratio of the corresponding GO, which could indicate the pronounced PPy conductivity over that of GO.

The changes in the dielectric constant (ε') and dielectric loss (ε''), with the frequency at different temperatures, are shown in Figures 6 and 7, respectively. The gradual decrease in these values by rising frequency could be discussed in the view of the Maxwell Wagner phenomena [43] to disturb the rotated dipoles with increasing frequency. The effect of GO and MZF inclusion on the dielectric properties of pure PPy could be achieved by comparing the prepared composites obtained dielectric values, with that of pure PPy (Figures 6 and 7). The obvious increase in the dielectric values, especially the dielectric

loss values (ε), indicated that the inclusion of these components into the PPy matrix could synergistically increase the dielectric properties. The π–π interactions developed by GO layers besides the dielectric characteristics of the MZF changed the polarization mode of the PPy matrix [28,44].

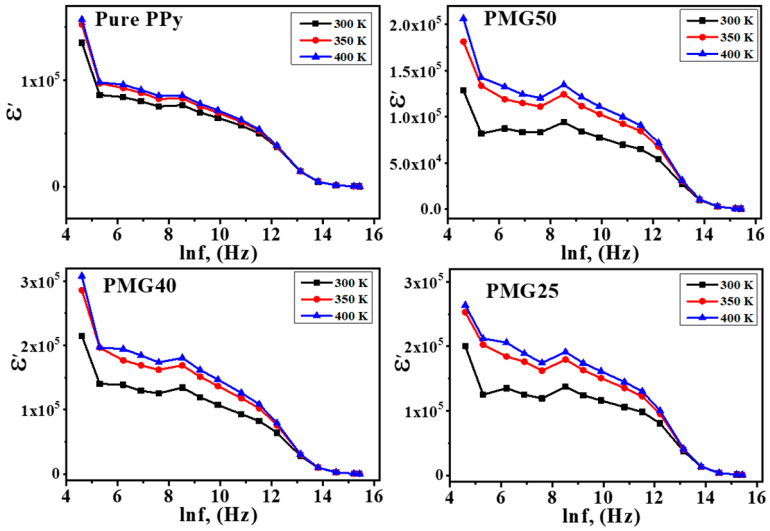

Figure 6. The dielectric constant (ε') versus frequency at different temperatures for pure PPy and PMG composites with different ratios.

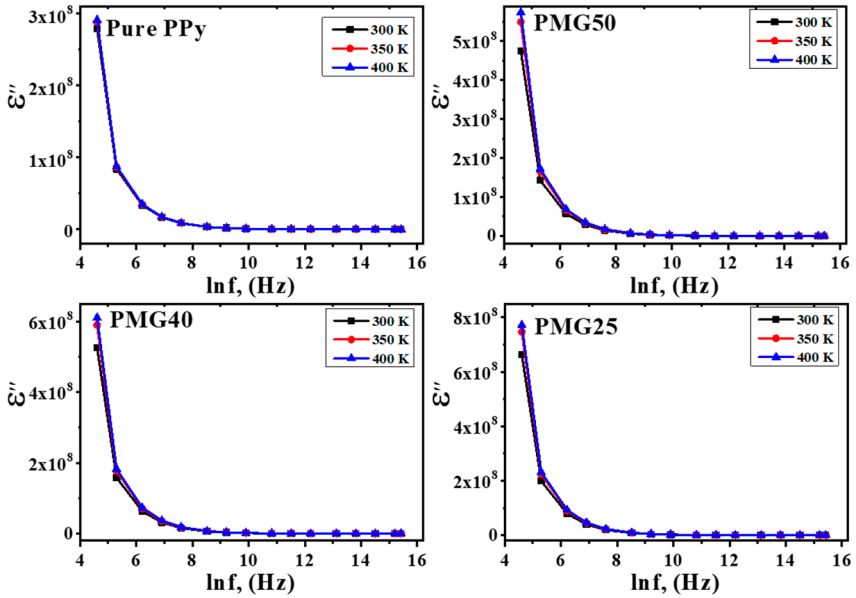

Figure 7. The dielectric loss (ε'') versus frequency at different temperatures for pure PPy and PMG composites with different ratios.

Generally, the obtained dielectric constant for all PMG composites appeared to be higher than those reported for similar polymeric composites GO/$MnFe_2O_4$/PPy [28]; this result could suggest the possibility of using MZF ferrite as an efficient dielectric material.

2.6. Adsorption/Dye Removal Capability

The existence of delocalized π-electrons besides oxygen-containing functional groups on GO, as well as amine groups on PPy surfaces, could facilitate the chelation and consequently, the adsorption removal of many environmental contaminants such as dyes [22–24]. In literature [1,2,18–21], magnetic spinels such as ferrites are extensively utilized in many

adsorbent composites because they can be easily separated under external magnetic fields. Unfortunately, in the present work, the magnetic properties of the ferrite component vanished due to the formation of the core-shell structure with the PPy matrix.

Figure 8 shows the UV-Vis absorption spectra of AR1 dye with and without PMG composites; it can be observed that the PMG50 has the highest efficiency compared with the other prepared composites, suggesting that increasing the GO ratio enhances adsorption, while increasing the PPy ratio inhibits it. This observation can be attributed to the high surface area of GO, alongside having enormous numbers of surface functional groups compared to PPy. In addition, the increase in the PPy ratio increases the coating capability of PPy for GO, thus shielding these functional groups, and thus decreasing their activity. According to this result, the composite PMG50 was utilized in all following experiments for studying the impacts of different parameters.

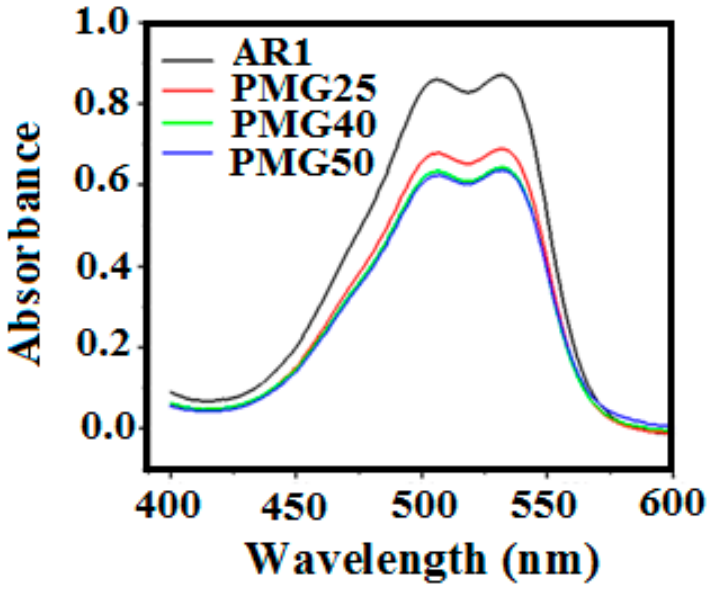

Figure 8. UV-Vis absorption spectra of AR1 dye with and without PMG composites.

The prepared PMG50 composite was, thus, investigated as an efficient adsorbent for the dye removal capability of AR1 from aqueous solutions. We studied the impact of different operating variables on removal efficiency, including pH, contact time, adsorbent dosage, and temperature. The kinetics of the adsorption process were then evaluated to establish a relation between adsorbed AR1 and adsorbent composites.

2.6.1. Effect of pH

Since AR1 dye is a negatively charged species, its adsorption is mainly influenced by the surface charge of PMG composite adsorbents and, in turn, by the solution pH [45]. It is well known that [46] at high pH values, the active sites on the adsorbents acquire negative charges, while, at lower values, the available protons will protonate the adsorbent surfaces; thus, increasing electrostatic attraction between negatively charged dye, and positively charged adsorbent sites [47]. The pH was varied between 2 and 11 (Experimental conditions: 50 mg PMG composite, 10 mL dye sample, 120 min contact time, 298 K, and AR1 concentration of 10 mg.L^{-1}). Figure 9a displays the change in the adsorption capacity vs. pH, from which we can conclude that the maximum adsorption capacity (75%) was at pH = 2.

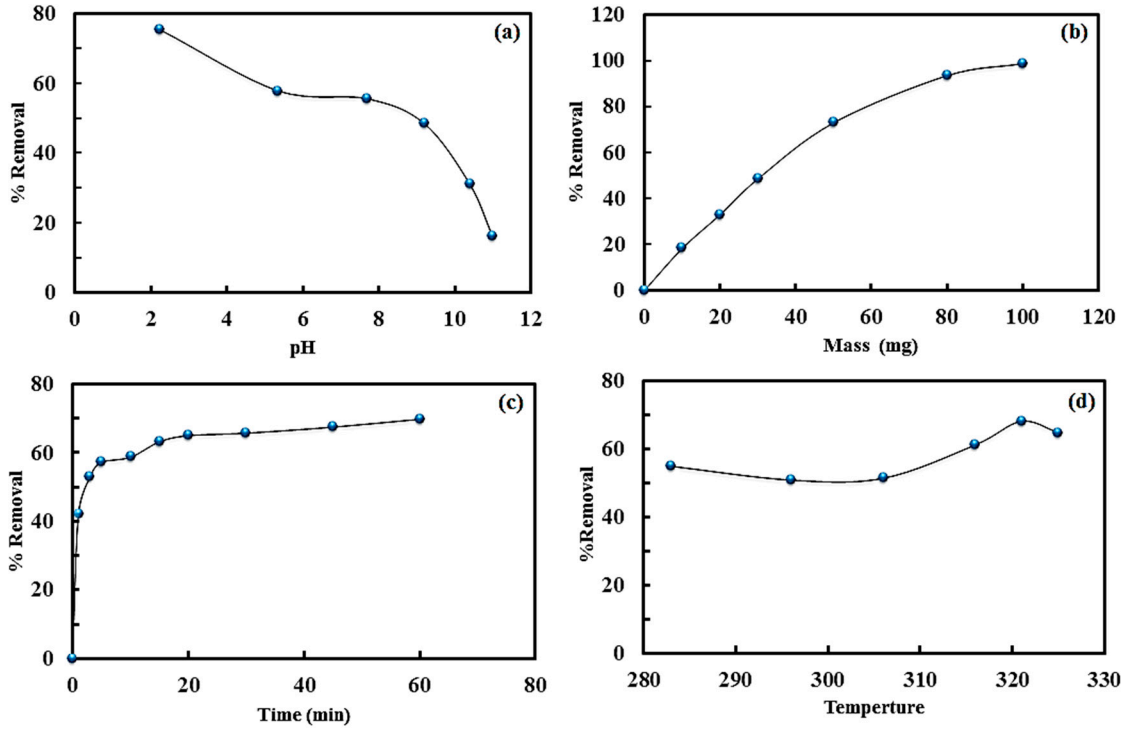

Figure 9. Effect of (**a**) pH, (**b**) PMG50 composite mass, (**c**) contact time, and (**d**) temperature on % adsorption removal of AR1 dye.

2.6.2. Effect of PMG Composite Dosage

The effectiveness of the PMG50 composite adsorbent mass on the elimination of AR1 from an aqueous solution was examined (Experimental conditions: 10, 20, 30, 50, 80, and 100 mg PMG50 composite, 10 mL dye sample, 120 min contact time, 298 K, and AR1 concentration of 10 mg.L^{-1}). Figure 9b showed that the removal capacity increases gradually by increasing composite mass from 73.1% to 98.8% with 50 mg and 100 mg of PMG50 composite, respectively, which could be attributed to the increase in the exposed surface area.

2.6.3. Effect of Contact Time

Figure 9c exhibited the adsorption capacity variation with the contact time starting from 1 to 60 min (Experimental conditions: 50 mg PMG50 composite, 10 mL dye sample, 298 K, and AR1 concentration of 10 mg.L^{-1}). The figure indicated rapid adsorption in the first 10 min with a removal efficiency of 58.8%, and reaching equilibrium at about 70% after 60 min. This behavior could be attributed to relatively high vacant surface-active sites at the beginning of adsorption.

2.6.4. Effect of Temperature

The temperature influence (283–325 K) on the adsorption rate of PMG50 composite for AR1 dye is shown in Figure 9d (Experimental conditions: 20 mg PMG50 composite, 10 mL dye sample, 120 min contact time, and dye concentration 10 mg.L^{-1}). From the figure, it is clear that the adsorption capacity increases with temperature due to the increase in the diffusion rate of ions [48].

Based on the above results, the optimal conditions for efficient AR1 dye removal using PMG50 composite were pH = 2, contact time of 60 min, PMG adsorbent dosage of 100 mg, and initial dye concentration of 10 mg.L^{-1}.

2.6.5. Adsorption Isotherm

The isotherm is a relationship between the equilibrium amount of dye adsorbed on PMG50 composite surfaces, and residual concentration in solution. The fitting of the adsorption data by analyzing them with different isotherm models is the most crucial step to understanding the interaction nature, and defining a suitable model to discuss the adsorption process. In the present work, the Lagergren pseudo-first-order kinetic model (PFO) [49] and pseudo-second-order kinetic rate (PSO) equations [50] were used to characterize the equilibrium adsorption. The linearized rate equations are [51]:

$$\ln(q_e - q_t) = \ln(q_e) - k_t t \quad (1)$$

$$\frac{t}{q_t} = \frac{t}{k_2 q_e^2} + \frac{t}{q_e} \quad (2)$$

where k_1 and k_2 (min^{-1}) represent PFO and PSO adsorption rate coefficients, the q_e and q_t represent the values at equilibrium and at any time t of the removed amounts per unit mass, respectively.

The suitability for modeling the entire adsorption process was estimated by plotting ln ($q_e - q_t$) and t/q_t vs. t (Figure 10a). The regression coefficients (R^2) of the obtained straight lines are listed in Table 2. The R^2 indicated the unsuitability of the PFO for modeling the adsorption process (R^2 = 0.847), while the excellent regression coefficient (R^2 = 0.999) for the PSO kinetic model (Figure 10b) suggested the applicability of this model to discuss the adsorption. Table 2 also summarizes q_e, k_1 and k_2 estimated from the slopes and intercepts of the two equations. The summarized results in Table 2 also showed that the amount of AR1 adsorbed per unit mass of PMG50 composite at equilibrium ($q_{e,calc}$) agrees well with the experimentally estimated values ($q_{e,exp}$) using the PSO model, which confirms this model to discuss adsorption.

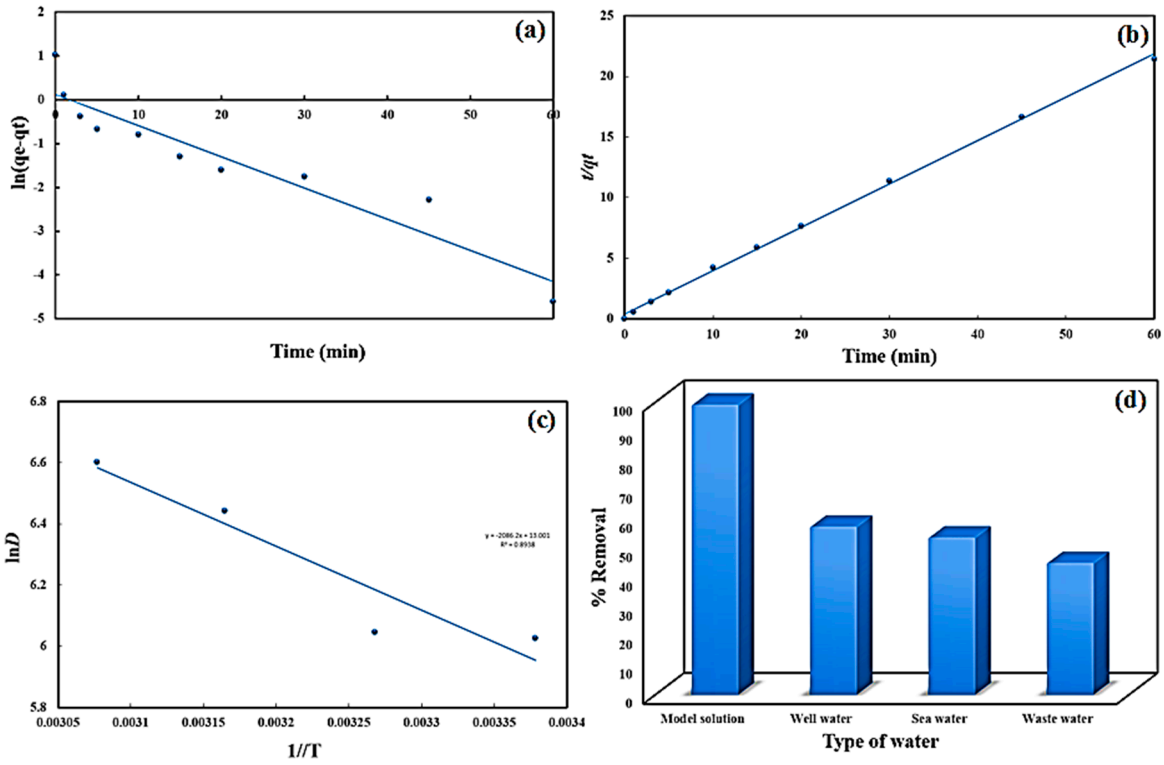

Figure 10. Kinetic models for the adsorption removal of AR1 by PMG50 composite. (**a**) PFO model and (**b**) PSO model. (**c**) the plot of ln D vs. $1/T$ for calculating thermodynamic parameters. (**d**) % removal of AR1 dye from different water sources.

Table 2. Kinetic model parameters for the adsorption of AR1 dye using PMG50 composite.

Parameters	Kinetic Model	
	PFO	PSO
K	0.071	0.320
$q_{e,exp}$ (mg/g)	2.806	2.806
$q_{e,cal}$ (mg/g)	1.130	2.798
R^2	0.847	0.999

Table 3 summarizes the performance of the PMG50 composite as an adsorbent for the removal adsorption of AR1 dye, compared with other already reported adsorbents according to their adsorption capacity and time [22,52–58]. From the table, it is clear that despite exhibiting better efficiencies than some of the reported adsorbents, it could be considered less efficient for the removal adsorption of AR1 dye compared to many others. Really, the relatively low efficiency adsorption capacity could be attributed to the complete coating of the PPy matrix for the other entire components (GO and MZF). As pointed out previously, this coating vanishes the magnetic sensitivities of the whole PMG composites, resulting in difficult separation besides coating the active adsorption sites on GO. In future work, this problem could be treated by decreasing the composite's PPy content ratio to a limit that would not affect the composites' improved electrical properties.

Table 3. Removal capacity and time for adsorption removal of AR1 dye using various adsorbents.

Material	Removal Capacity (mg/g)	Time	Reference
Chitosan/graphene nanoplates	60.49	60 min	[52]
Raw Indonesian kaolin clay	12.80	90 min	[53]
Activated carbons	57.10	150 min	[54]
Peel of Cucumis sativus fruit	18.76	24 h	[55]
Modified titanate nanotubes	2.58	30 min	[56]
Hybrid adsorbents of tannin and APTES	418.30	8 h	[57]
Organic-inorganic hybrid clay	397.0	5 h	[58]
MZF/GO magnetic nanocomposite	49.90	40 min	[22]
PMG 50 composite	2.81	60 min	Present work

2.6.6. Thermodynamic Studies

The spontaneity and suitability of the entire adsorption process were estimated thermodynamically by calculating the changes in Gibbs free energy (ΔG), enthalpy (ΔH), and entropy (ΔS) according to the following equations [51]:

$$D = \frac{q_e}{C_e} \quad (3)$$

$$logD = \frac{\Delta S}{R} - \frac{\Delta H}{2.303\ RT} \quad (4)$$

$$\Delta G = \Delta H - T\Delta S \quad (5)$$

where q_e is the equilibrium amount of AR1 adsorbed per unit mass of PMG50 composite (mg/g), and C_e is the equilibrium concentration of AR1 in solution (mg.L^{-1}). ΔH and ΔS could be calculated by plotting log D vs. 1/T, as shown in Figure 10c, the slope, and the intercept; then, the ΔG was calculated to be 298 K from equation 5.

The calculated values are −14.85 kJ/mol, 17.34 J/mol.K, and 0.11 kJ/mol for the ΔG, ΔH, and ΔS, respectively (Table 3). The negative ΔG confirmed the spontaneity of the adsorption process. In contrast, the negative enthalpy indicates the endothermic nature of

the adsorption, and the positive entropy could suggest an increase in the degree of freedom at the solid–liquid interface.

2.6.7. Environmental Applications

Environmental application of the entire adsorbent, PMG50 composite, was investigated through the remediation of AR1 from real samples of different environmental water, including seawater collected from the Red Sea, Jeddah, Saudi Arabia; wastewater collected from Membrane Bio-Reactor Technology Wastewater Treatment Plant; King Abdulaziz University, Jeddah; and healthy water collected from deep well near Jeddah. Figure 10d exhibited % AR1 dye removal from different water sources. Since AR1 concentration in these water sources is almost zero, the water samples were spiked with AR1 dye to achieve 25 mg.L^{-1} to simulate the pollution scenario.

The PMG50 composite was then added. The % removal of AR1 was 53.7%, 45.0%, and 57.4% for seawater, wastewater, and healthy water, respectively. These results indicated that the PMG50 composite removed most AR1. The smaller removal efficiencies of these values, compared to the model solution, could be attributed to the excessive concentrations of different ions such as Na^+, K^+, Mg^{2+}, and Ca^{2+}, which already exist in seawater; there is a probability that there are other organic and inorganic pollutants present in wastewater. These contaminants may compete or cause a screening effect on the adsorption sites located at PMG50 composite surfaces, and thus are expected to reduce AR1 adsorption.

2.6.8. Probable Mechanism

The most common physicochemical interactions required for dye adsorption include electrostatic interactions, ion exchange, inner-sphere surface complexation, and p-p stacking [59]. The chemical adsorption (chemisorption) is attributed to the strong chemical bonding when the PMG shares electron pairs with the adsorbates AR1. In contrast, physical adsorption (physisorption) results from weak attractive forces (e.g., van der Waals, dipole–dipole interactions, hydrogen bonding, etc.) between PMG and adsorbates (AR1) [60]. The AR1 dye was strongly bound to (PMG) through hydrogen bonding and electrostatic interactions between the surface functional groups (S-CO=O, S-N=N+] and S-COOH, where S represents the surface of the (PMG) and AR1 dye. An illustration of the possible interactions between AR1 dye and PMG 50 is shown in Figure 11.

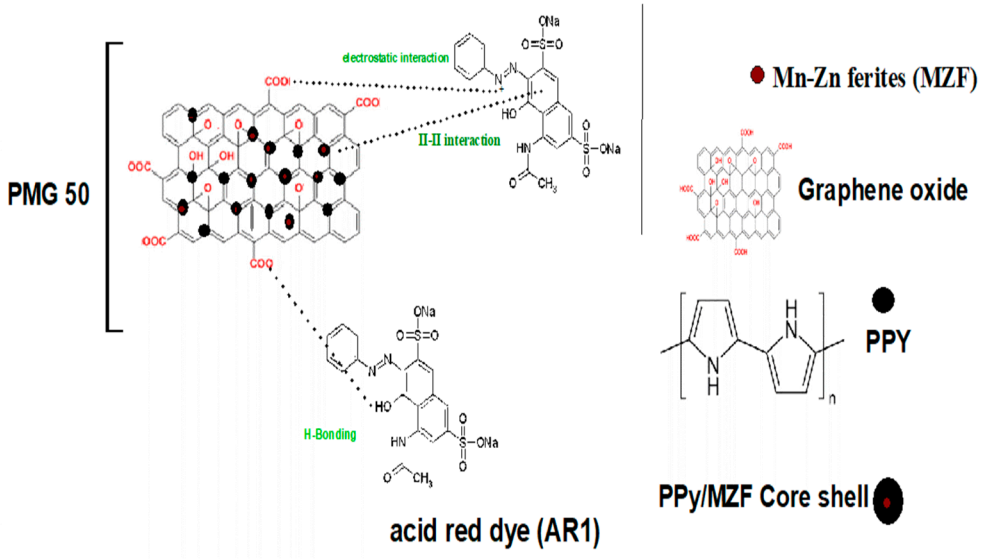

Figure 11. Probable adsorption mechanisms of acid red 1 (AR1) dye on PMG50 ternary composites.

3. Experimental

3.1. Materials

Extracted filtrate of SZCBs was obtained as explained in our previous publications [30,61], and used with nitrates: $Fe(NO_3)_2 \cdot 9H_2O$, $Mn(NO_3)_2 \cdot 4H_2O$, and $Zn(NO_3)_2 \cdot 6H_2O$ (BDH, Poole, UK) and commercial sucrose; $C_{12}H_{22}O_{11}$ to prepare $Mn_{0.8}Zn_{0.2}Fe_2O_4$. Graphite powder (Sigma Aldrich, Munich, Germany), $NaNO_3$, $KMnO_4$, H_2O_2, and H_2SO_4 (BDH, Poole, UK) were used to prepare the GO. A 0.5 M HCl (Sigma Aldrich, Munich, Germany) and ammonium persulphate (APS) $(NH_4)_2S_2O_8$ (BDH, Poole, UK) were used to polymerize pyrrole monomer (C_4H_5N) into PPy.

AR1 belongs to the group of azo dyes since it contains an azo group band (-N=N-). The molecular structure provided by PubChem is shown in Figure 12; its molar mass is 509.4 g mol^{-1} with the molecular formula $C_{18}H_{13}N_3Na_2O_8S_2$. The stock solution was prepared by dissolving 500 mg in 1000 mL of deionized water, and lower concentrations were prepared via dilution.

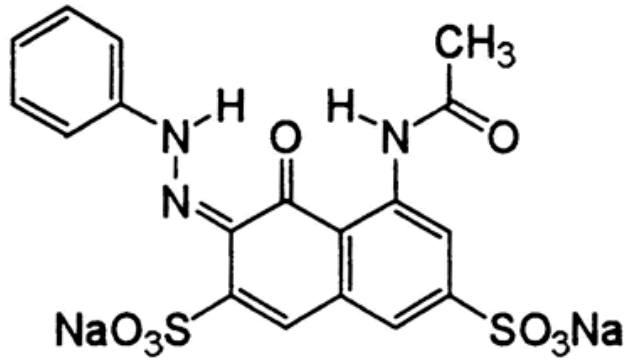

Figure 12. The molecular structure provided by PubChem for AR1.

3.2. Preparation of MZF Nanoparticles

MZF nanoparticles were prepared using materials from SZCBs via the sucrose sol-gel auto-combustion technique [61]. In brief, the proper metal ratios were adjusted using nitrates and stirred at 60 °C, followed by the addition of sucrose fuel after setting the solution pH to 7 using ammonium hydroxide. The formed gel began after aging at about 100 °C; then, it was auto-combusted to form the entire ferrite.

3.3. Preparation of GO

Modified Hummers' method [31] was used to prepare GO powder. Briefly, 1 g graphite, 0.5 g $NaNO_3$, and 100 mL H_2SO_4 were mixed at 0 °C for 2 h. After slowly adding 6 g $KMnO_4$, the solution temperature was raised to 35 °C. After 12 h, deionized water gradually maintained at the temperature near 2°C. After 1 h stirring, 30% H_2O_2 was added slowly to remove the residual $KMnO_4$ and MnO_2. GO was then obtained by centrifuging and washing (5% HCl) several times. Finally, it was dispersed in 0.5 M HCl under sonication for 1 h to exfoliate the obtained GO.

3.4. Preparation of PPy

The PPy was prepared via the oxidative polymerization of pyrrole [32]. A total of 100 mL of 0.5 M HCl was stirred with 1 g pyrrole monomer in an ice bath for 15 min, before adding 2.6 g APS. The solution was then stirred at 0 °C under a nitrogen atmosphere for 24 h. The formed PPy black precipitate was washed using water, and dried.

3.5. Preparation of PMG Ternary Composites

Ternary composites, PMG with different weight ratios (*wt*/*wt*) of 25:25:50 (PMG50), 35:25:40 (PMG40), and 55:20:25 (PMG25) were prepared using the in situ polymerization technique [38]. In a typical experiment, the exact ratio of MZF previously prepared via

sucrose auto-combustion was mixed thoroughly with a stoichiometric amount of GO in 0.5 M HCl (100 mL) under vigorous sonication at room temperature for 1 h. The calculated equivalent ratio of pyrrole monomer was then added to the sonicated mixture under a continuous flow of nitrogen gas, keeping the temperature at about 0 °C. After that, a 2.6 g APS was dissolved in 25 mL HCl (0.5 M) and added dropwise. The mixture was kept stirring overnight and filtered, and the obtained black precipitate was washed with water and dried. Figure 13 displays a schematic diagram for preparing the PMG ternary nanocomposites.

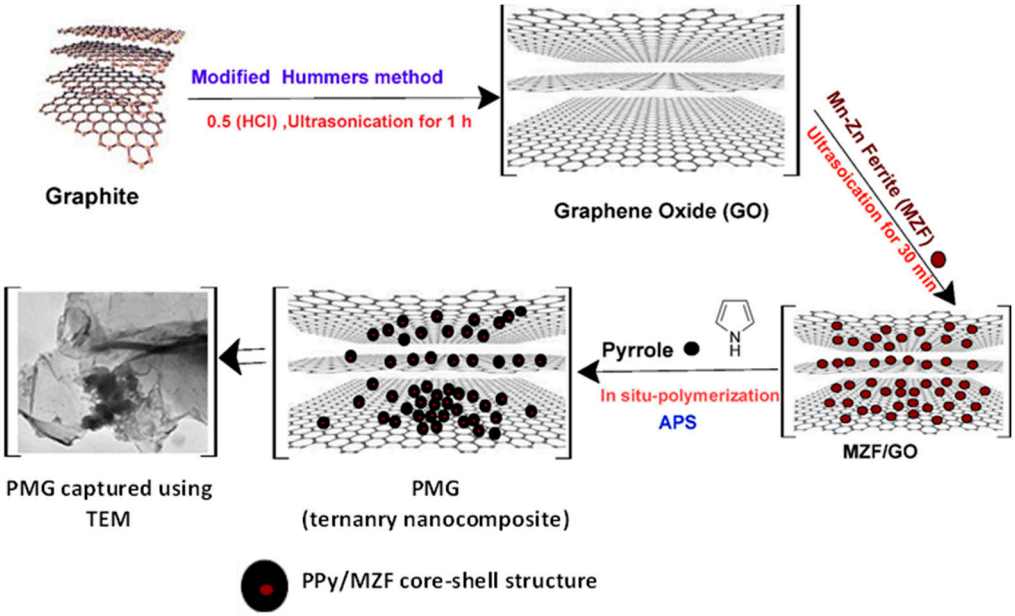

Figure 13. The schematic diagram for illustration of the PMG ternary nanocomposite synthesis.

3.6. Adsorption Experiments

Adsorption experiments were performed to investigate the removal capability of the prepared composites for AR1 in aqueous solutions. In a typical experiment, 20 mL of 20 ppm AR1 dye was treated with a definite weight of PMG composites for a certain time. The amount of the adsorbed AR1 dye was determined using a UV-VIS spectrophotometer, and the following equation [62]:

$$\% \text{ Dye removed} = 100 - \frac{C_t}{C_0} \times 100\% \quad (6)$$

where C_0 and C_t are concentrations of AR1 in solution (mg/L) at the beginning of the adsorption and after time t, respectively.

The influence of different experimental conditions viz; mass, pH, initial dye concentration, temperature as well as ionic strength were investigated to determine the dye removal performance of PMG composites. Different doses of adsorbent (10, 20, 30, 50, 80, and 100 mg) per 10 mL of dye solution were utilized. The pH value between 2 and 11 was adjusted using 1 M HCl or NaOH. The contact time was set up to 1 h, and temperatures between 200 and 300 K were used to study the kinetic experiments.

3.7. Characterization

Crystallite structures of PMG composites were examined using X-ray diffraction (XRD), model D8 Advance (Bruker, Billerica, Massachusetts, USA). Fourier transform infrared (FT-IR) spectra were monitored using an FT-IR spectrometer, the ALPHA II model (Bruker, Billerica, Massachusetts, USA). A morphological study was explored using a transmission electron microscope (TEM) model JEOL 2010 (JEOL, Tokyo, Japan). Magnetic

hysteresis at room temperature was recorded using a vibrating sample magnetometer, model VSM-8600M (Quantum Design Inc., San Diego, California, USA). The ac-conductivity and dielectric properties were measured using pressed pellets with an LCR bridge, model Hioki LCR 3531 (HIOKI, Nagano, Japan). PerkinElmer UV/VIS/NIR spectrometer, model LAMBDA 1050 (PerkinElmer Inc, Waltham, Massachusetts, USA), was used to monitor the change in the UV-VIS spectra of AR1 in the aqueous solution with time.

4. Conclusions

PMG composites with different ratios were successfully prepared via the in situ polymerization process of pyrrole. The MZF content was prepared using materials from SZCBs, acid leaching, and sucrose auto-combustion, while GO was synthesized via oxidation and exfoliation of graphite. XRD and FT-IR studies showed only the characteristic XRD peaks and FTIR spectral bands attributed to PPy, indicating the complete coating of GO and MZF with the PPy matrix. This complete coating vanished the magnetic characteristics of the MZF ferrite content, as presented through VSM measurements. The presence of GO and MZF decreased the thermal stability of PPy, also increasing its conductivity and dielectric properties. The PMG composites were investigated as efficient adsorbents for the dye removal capability of AR1 from solutions, and the PMG50 was found to be the more efficient ratio for better dye removal. The analysis of the adsorption data suggested the applicability of the PSO kinetic model in discussing adsorption. The observed low efficiency for the removal of AR1, compared to other materials in the literature, could be attributed to the complete coating of the PPy matrix for the GO having numerous active sites available for adsorption. In future work, this problem could be treated by decreasing the PPy content ratio in the composite to avoid this issue.

Author Contributions: All authors contributed to the study's conception and design. M.A.G.: conceptional, methodology; formal analysis; investigation; supervision, data curation; writing—original draft. E.A.A.-H.: methodology; formal analysis; investigation; resources; review and editing. Y.M.A.A.: validation; writing—review and editing. M.A.S.: investigation; validation; writing—review and editing. A.A.: validation; writing—review and editing. A.A.A.-J.: validation; writing—review and editing. A.S.: investigation; data curation; writing—review and editing. All authors commented on previous versions of the manuscript. All authors have read and agreed to the published version of the manuscript.

Funding: This research received no external funding.

Data Availability Statement: Data and materials will be available on demand.

Conflicts of Interest: The authors declare no conflict of interest.

References

1. Xiang, B.; Ling, D.; Lou, H.; Gu, H. 3D hierarchical flower-like nickel ferrite/manganese dioxide toward lead (II) removal from aqueous water. *J. Hazard. Mater.* **2017**, *325*, 178–188. [CrossRef] [PubMed]
2. Wang, W.; Cai, K.; Wu, X.; Shao, X.; Yang, X. A novel poly(m-phenylenediamine)/reduced graphene oxide/nickel ferrite magnetic adsorbent with excellent removal ability of dyes and Cr(VI). *J. Alloy. Compd.* **2017**, *722*, 532–543. [CrossRef]
3. Almashhori, K.; Ali, T.T.; Saeed, A.; Alwafi, R.; Aly, M.; Al-Hazmi, F.E. Antibacterial and photocatalytic activities of controllable (anatase/rutile) mixed phase TiO_2 nanophotocatalysts synthesized via a microwave-assisted sol–gel method. *New J. Chem.* **2020**, *44*, 562–570. [CrossRef]
4. Wali, L.A.; Alwan, A.M.; Dheyab, A.B.; Hashim, D.A. Excellent fabrication of Pd-Ag NPs/PSi photocatalyst based on bimetallic nanoparticles for improving methylene blue photocatalytic degradation. *Optik* **2019**, *179*, 708–717. [CrossRef]
5. Wang, G.; Chang, J.; Tang, W.; Xie, W.; Ang, Y.S. 2D materials and heterostructures for photocatalytic water-splitting: A theoretical perspective. *J. Phys. D Appl. Phys.* **2022**, *55*, 293002. [CrossRef]
6. Bagheri, N.; Mansour Lakouraj, M.; Hasantabar, V.; Mohseni, M. Biodegradable macro-porous CMC-polyaniline hydrogel: Synthesis, characterization and study of microbial elimination and sorption capacity of dyes from waste water. *J. Hazard. Mater.* **2021**, *403*, 123631. [CrossRef]
7. Iqbal, M.Z.; Abdala, A.A. Thermally reduced graphene: Synthesis, characterization and dye removal applications. *RSC Adv.* **2013**, *3*, 24455–24464. [CrossRef]

8. Adel, M.; Ahmed, M.A.; Mohamed, A.A. Effective removal of indigo carmine dye from wastewaters by adsorption onto mesoporous magnesium ferrite nanoparticles. *Environ. Nanotechnol. Monit. Manag.* **2021**, *16*, 100550. [CrossRef]
9. Jayalakshmi, R.; Jeyanthi, J.; Aswin Sidhaarth, K.R. Versatile application of cobalt ferrite nanoparticles for the removal of heavy metals and dyes from aqueous solution. *Environ. Nanotechnol. Monit. Manag.* **2022**, *17*, 100659. [CrossRef]
10. Bayantong, A.R.B.; Shih, Y.-J.; Ong, D.C.; Abarca, R.R.M.; Dong, C.-D.; de Luna, M.D.G. Adsorptive removal of dye in wastewater by metal ferrite-enabled graphene oxide nanocomposites. *Chemosphere* **2021**, *274*, 129518. [CrossRef]
11. Zhao, X.; Wang, W.; Zhang, Y.; Wu, S.; Li, F.; Liu, J.P. Synthesis and characterization of gadolinium doped cobalt ferrite nanoparticles with enhanced adsorption capability for Congo Red. *Chem. Eng. J.* **2014**, *250*, 164–174. [CrossRef]
12. Wang, W.; Ding, Z.; Wu, S.; Li, F.; Ping Liu, J. Ethanol-assisted synthesis and adsorption property of flake-like $NiFe_2O_4$ nanoparticles. *Ceram. Int.* **2015**, *41*, 13624–13629. [CrossRef]
13. Ding, Z.; Wang, W.; Zhang, Y.; Li, F.; Liu, J.P. Synthesis, characterization and adsorption capability for Congo red of $CoFe_2O_4$ ferrite nanoparticles. *J. Alloy. Compd.* **2015**, *640*, 362–370. [CrossRef]
14. Liu, J.; Zeng, M.; Yu, R. Surfactant-free synthesis of octahedral $ZnO/ZnFe_2O_4$ heterostructure with ultrahigh and selective adsorption capacity of malachite green. *Sci. Rep.* **2016**, *6*, 25074. [CrossRef]
15. Wu, X.; Ding, Z.; Wang, W.; Song, N.; Khaimanov, S.; Tsidaeva, N. Effect of polyacrylic acid addition on structure, magnetic and adsorption properties of manganese ferrite nanoparticles. *Powder Technol.* **2016**, *295*, 59–68. [CrossRef]
16. Meng, Y.; Chen, D.; Sun, Y.; Jiao, D.; Zeng, D.; Liu, Z. Adsorption of Cu^{2+} ions using chitosan-modified magnetic Mn ferrite nanoparticles synthesized by microwave-assisted hydrothermal method. *Appl. Surf. Sci.* **2015**, *324*, 745–750. [CrossRef]
17. Oyetade, O.A.; Nyamori, V.O.; Martincigh, B.S.; Jonnalagadda, S.B. Effectiveness of carbon nanotube–cobalt ferrite nanocomposites for the adsorption of rhodamine B from aqueous solutions. *RSC Adv.* **2015**, *5*, 22724–22739. [CrossRef]
18. Gabal, M.A.; Abou Zeid, K.M.; El-Gendy, A.A.; El-Shall, M.S. One-step novel synthesis of $CoFe_2O_4$/graphene composites for organic dye removal. *J. Sol-Gel Sci. Technol.* **2019**, *89*, 743–753. [CrossRef]
19. Gabal, M.A.; Al-Zahrani, N.G.; Al Angari, Y.M.; Al-Juaid, A.A.; Abdel-Fadeel, M.A.; Alharbi, S.R.; El-Shishtawy, R.M. CoFe2O4/MWCNTs nano-composites structural, thermal, magnetic, electrical properties and dye removal capability. *Mater. Res. Express* **2019**, *6*, 105059. [CrossRef]
20. Gabal, M.A.; Al-Juaid, A.A.; El-Rashed, S.; Hussein, M.A.; Al Angari, Y.M.; Saeed, A. Structural, Thermal, Magnetic and Electrical Properties of Polyaniline/$CoFe_2O_4$ Nano-composites with Special Reference to the Dye Removal Capability. *J. Inorg. Organomet. Polym. Mater.* **2019**, *29*, 2197–2213. [CrossRef]
21. Gabal, M.A.; Al-Harthy, E.A.; Al Angari, Y.M.; Abdel Salam, M. MWCNTs decorated with Mn0.8Zn0.2Fe2O4 nanoparticles for removal of crystal-violet dye from aqueous solutions. *Chem. Eng. J.* **2014**, *255*, 156–164. [CrossRef]
22. Salam, M.A.; Gabal, M.A.; Al Angari, Y.M. The recycle of spent Zn–C batteries and the synthesis of magnetic nanocomposite from graphene nanosheets and ferrite and its application for environmental remediation. *J. Mater. Res. Technol-JMRT* **2022**, *18*, 4267–4276. [CrossRef]
23. Nag, S.; Ghosh, A.; Das, D.; Mondal, A.; Mukherjee, S. $Ni_{0.5}Zn_{0.5}Fe_2O_4$/polypyrrole nanocomposite: A novel magnetic photocatalyst for degradation of organic dyes. *Synth. Met.* **2020**, *267*, 116459. [CrossRef]
24. Huang, F.; Tian, X.; Wei, W.; Xu, X.; Li, J.; Guo, Y.; Zhou, Z. Wheat straw-core hydrogel spheres with polypyrrole nanotubes for the removal of organic dyes. *J. Clean. Prod.* **2022**, *344*, 131100. [CrossRef]
25. Ding, L.; Zhao, X.; Huang, Y.; Yan, J.; Li, T.; Liu, P. Ultra-broadband and covalently linked core–shell CoFe2O4@PPy nanoparticles with reduced graphene oxide for microwave absorption. *J. Colloid Interface Sci.* **2021**, *595*, 168–177. [CrossRef]
26. Mariappan, C.R.; Gajraj, V.; Gade, S.; Kumar, A.; Dsoke, S.; Indris, S.; Ehrenberg, H.; Prakash, G.V.; Jose, R. Synthesis and electrochemical properties of rGO/polypyrrole/ferrites nanocomposites obtained via a hydrothermal route for hybrid aqueous supercapacitors. *J. Electroanal. Chem.* **2019**, *845*, 72–83. [CrossRef]
27. Hussain, H.V.; Ahmad, M.; Ansar, M.T.; Mustafa, G.M.; Ishaq, S.; Naseem, S.; Murtaza, G.; Kanwal, F.; Atiq, S. Polymer based nickel ferrite as dielectric composite for energy storage applications. *Synth. Met.* **2020**, *268*, 116507. [CrossRef]
28. Riaz, A.; ul Ain, Q.; Kanwal, F.; Ishaq, S.; Khan, A.R.; Mustafa, G.M.; Abbas, S.K.; Naseem, S.; Ramay, S.M.; Atiq, S. Identification of frequency regimes for short and long range mobility of charge carriers in GO/$MnFe_2O_4$/PPy nanocomposites. *Synth. Met.* **2020**, *263*, 116336. [CrossRef]
29. Thu, T.V.; Van Nguyen, T.; Le, X.D.; Le, T.S.; Van Thuy, V.; Huy, T.Q.; Truong, Q.D. Graphene-MnFe2O4-polypyrrole ternary hybrids with synergistic effect for supercapacitor electrode. *Electrochim. Acta* **2019**, *314*, 151–160. [CrossRef]
30. Gabal, M.A.; Al-Harthy, E.A.; Al Angari, Y.M.; Awad, A.; Al-Juaid, A.A.; Abdel-Daiem, A.M.; Saeed, A. Recovery of $Mn_{0.8}Zn_{0.2}Fe_2O_4$ from Zn–C battery: Auto-combustion synthesizes, characterization, and electromagnetic properties. *J. Sol-Gel Sci. Technol.* **2021**, *100*, 526–537. [CrossRef]
31. Hummers, W.S., Jr.; Offeman, R.E. Preparation of Graphitic Oxide. *J. Am. Chem. Soc.* **1958**, *80*, 1339. [CrossRef]
32. Chougulea, M.A.; Pawara, S.G.; Godsea, P.R.; Mulika, R.N.; Senb, S.; Patila, V.B. Synthesis and Characterization of Polypyrrole (PPy) Thin Films. *Soft Nanosci. Lett.* **2011**, *1*, 6–10. [CrossRef]
33. He, H.; Klinowski, J.; Forster, M.; Lerf, A. A new structural model for graphite oxide. *Chem. Phys. Lett.* **1998**, *287*, 53–56. [CrossRef]
34. Johra, F.T.; Lee, J.-W.; Jung, W.-G. Facile and safe graphene preparation on solution based platform. *J. Ind. Eng. Chem.* **2014**, *20*, 2883–2887. [CrossRef]

35. Aigbe, U.O.; Das, R.; Ho, W.H.; Srinivasu, V.; Maity, A. A novel method for removal of Cr(VI) using polypyrrole magnetic nanocomposite in the presence of unsteady magnetic fields. *Sep. Purif. Technol.* **2018**, *194*, 377–387. [CrossRef]
36. Seo, I.; Pyo, M.; Cho, G. Micrometer to Nanometer Patterns of Polypyrrole Thin Films via Microphase Separation and Molecular Mask. *Langmuir* **2002**, *18*, 7253–7257. [CrossRef]
37. Liao, Y.; Li, X.-G.; Kaner, R.B. Facile Synthesis of Water-Dispersible Conducting Polymer Nanospheres. *ACS Nano* **2010**, *4*, 5193–5202. [CrossRef]
38. Gabal, M.A.; Al-Harthy, E.A.; Al Angari, Y.M.; Awad, A.; Al-Juaid, A.A.; Hussein, M.A.; Abdel-Daiem, A.M.; Sobahi, T.R.; Saeed, A. Synthesis, Structural, Magnetic and High-Frequency Electrical Properties of $Mn_{0.8}Zn_{0.2}Fe_2O_4$/Polypyrrole Core–Shell Composite Using Waste Batteries. *J. Inorg. Organomet. Polym. Mater.* **2022**, *32*, 1975–1987. [CrossRef]
39. Fan, W.; Zhang, C.; Tjiu, W.W.; Pramoda, K.P.; He, C.; Liu, T. Graphene-Wrapped Polyaniline Hollow Spheres As Novel Hybrid Electrode Materials for Supercapacitor Applications. *ACS Appl. Mater. Interfaces* **2013**, *5*, 3382–3391. [CrossRef]
40. Jiang, L.; Dong, C.; Jin, B.; Wen, Z.; Jiang, Q. ZnFe2O4@PPy core-shell structure for high-rate lithium-ion storage. *J. Electroanal. Chem.* **2019**, *851*, 113442. [CrossRef]
41. Raghuram, N.; Rao, T.S.; Naidu, K.C.B. Magnetic properties of hydrothermally synthesized $Ba_{1-x}SrxFe_{12}O_{19}$ (x = 0.0–0.8) nanomaterials. *Appl. Phys. A* **2019**, *125*, 839. [CrossRef]
42. Sagar, T.V.; Rao, T.S.; Naidu, K.C.B. Effect of calcination temperature on optical, magnetic and dielectric properties of Sol-Gel synthesized $Ni_{0.2}Mg_{0.8-x}ZnxFe_2O_4$ (x = 0.0–0.8). *Ceram. Int.* **2020**, *46*, 11515–11529. [CrossRef]
43. Iwamoto, M. Maxwell–Wagner Effect. In *Encyclopedia of Nanotechnology*; Bhushan, B., Ed.; Springer: Dordrecht, The Netherlands, 2012; pp. 1276–1285. [CrossRef]
44. He, Z.-Z.; Yu, X.; Yang, J.-H.; Zhang, N.; Huang, T.; Wang, Y.; Zhou, Z.-W. Largely enhanced dielectric properties of poly(vinylidene fluoride) composites achieved by adding polypyrrole-decorated graphene oxide. *Compos. Part A: Appl. Sci. Manuf.* **2018**, *104*, 89–100. [CrossRef]
45. Moghaddam, S.S.; Moghaddam, A.M.; Arami, M. A comparative study of acid red 119 dye adsorption onto dried sewage sludge and sewage sludge ash: Isotherm, kinetic and desorption study. *J. Residuals Sci. Techn.* **2010**, *7*, 199–207.
46. Smitha, T.; Thirumalisamy, S.; Manonmani, S. Equilibrium and Kinetics Study of Adsorption of Crystal Violet onto the Peel of *Cucumis sativa* Fruit from Aqueous Solution. *E-J. Chem.* **2012**, *9*, 457632. [CrossRef]
47. Akkaya, G.; Özer, A. Biosorption of Acid Red 274 (AR 274) on Dicranella varia: Determination of equilibrium and kinetic model parameters. *Process Biochem.* **2005**, *40*, 3559–3568. [CrossRef]
48. Peng, W.; Li, H.; Liu, Y.; Song, S. A review on heavy metal ions adsorption from water by graphene oxide and its composites. *J. Mol. Liq.* **2017**, *230*, 496–504. [CrossRef]
49. Zur Theorie der sogenannten Adsorption gelöster Stoffe. *Z. Für Chem. Und Ind. Der Kolloide* **1907**, *2*, 15. [CrossRef]
50. Rudzinski, W.; Plazinski, W. On the applicability of the pseudo-second order equation to represent the kinetics of adsorption at solid/solution interfaces: A theoretical analysis based on the statistical rate theory. *Adsorption* **2009**, *15*, 181–192. [CrossRef]
51. Owija, N.Y.; Kosa, S.A.; Abdel Salam, M. Removal of cadmium ions from aqueous solution by zero valent iron nanoparticles: Equilibrium and thermodynamic studies. *J. Mol. Liq.* **2021**, *342*, 117462. [CrossRef]
52. Zhang, C.; Chen, Z.; Guo, W.; Zhu, C.; Zou, Y. Simple fabrication of Chitosan/Graphene nanoplates composite spheres for efficient adsorption of acid dyes from aqueous solution. *Int. J. Biol. Macromol.* **2018**, *112*, 1048–1054. [CrossRef] [PubMed]
53. Ashrul Asbollah, M.; Sahid, M.S.M.; Padmosoedarso, K.M.; Mahadi, A.H.; Kusrini, E.; Hobley, J.; Usman, A. Individual and Competitive Adsorption of Negatively Charged Acid Blue 25 and Acid Red 1 onto Raw Indonesian Kaolin Clay. *Arab. J. Sci. Eng.* **2022**, *47*, 6617–6630. [CrossRef]
54. Thinakaran, N.; Panneerselvam, P.; Baskaralingam, P.; Elango, D.; Sivanesan, S. Equilibrium and kinetic studies on the removal of Acid Red 114 from aqueous solutions using activated carbons prepared from seed shells. *J. Hazard. Mater.* **2008**, *158*, 142–150. [CrossRef]
55. Khanna, S.; Rattan, V.K. Removal of acid red 1 from aqueous waste streams using peel of cucumis sativus fruit. Equilibrium studies. *J. Chem. Techn. Metall.* **2017**, *52*, 803–811.
56. Juang, L.-C.; Lee, C.-K.; Wang, C.-C.; Hung, S.-H.; Lyu, M.-D. Adsorptive Removal of Acid Red 1 from Aqueous Solution with Surfactant Modified Titanate Nanotubes. *Environ. Eng. Sci.* **2008**, *25*, 519–528. [CrossRef]
57. Leite, A.J.B.; Lima, E.C.; dos Reis, G.S.; Thue, P.S.; Saucier, C.; Rodembusch, F.S.; Dias, S.L.P.; Umpierres, C.S.; Dotto, G.L. Hybrid adsorbents of tannin and APTES (3-aminopropyltriethoxysilane) and their application for the highly efficient removal of acid red 1 dye from aqueous solutions. *J. Environ. Chem. Eng.* **2017**, *5*, 4307–4318. [CrossRef]
58. Thue, P.S.; Sophia, A.C.; Lima, E.C.; Wamba, A.G.N.; de Alencar, W.S.; dos Reis, G.S.; Rodembusch, F.S.; Dias, S.L.P. Synthesis and characterization of a novel organic-inorganic hybrid clay adsorbent for the removal of acid red 1 and acid green 25 from aqueous solutions. *J. Clean. Prod.* **2018**, *171*, 30–44. [CrossRef]
59. Reddy, D.H.K.; Yun, Y.-S. Spinel ferrite magnetic adsorbents: Alternative future materials for water purification? *Coord. Chem. Rev.* **2016**, *315*, 90–111. [CrossRef]
60. Sanghi, R.; Verma, P. Decolorisation of aqueous dye solutions by low-cost adsorbents: A review. *Color. Technol.* **2013**, *129*, 85–108. [CrossRef]

61. Gabal, M.A.; Al-luhaibi, R.S.; Al Angari, Y.M. Mn–Zn nano-crystalline ferrites synthesized from spent Zn–C batteries using novel gelatin method. *J. Hazard. Mater.* **2013**, *246–247*, 227–233. [CrossRef]
62. Manohar, A.; Krishnamoorthi, C.; Naidu, K.C.B.; Narasaiah, B.P. Dielectric, Magnetic Hyperthermia and Photocatalytic Properties of $Mg_{0.7}Zn_{0.3}Fe_2O_4$ Nanocrystals. *IEEE Trans. Magn.* **2020**, *56*, 5200207. [CrossRef]